

# Unveiling the Electronic Origin of Anomalous Contact Conductance in Twisted Bilayer Graphene

Kevin J. U. Vidarte,<sup>1</sup> Caio Lewenkopf,<sup>1</sup> F. Crasto de Lima,<sup>2</sup>  
R. Hiroki Miwa,<sup>3</sup> Felipe Pérez Rizzo,<sup>4</sup> and Eric Suárez Morell<sup>4</sup>

<sup>1</sup>*Instituto de Física, Universidade Federal do Rio de Janeiro, 21941-972 Rio de Janeiro, RJ, Brazil*

<sup>2</sup>*Ilum School of Science, Brazilian Center for Research in Energy and Materials (CNPEM), Campinas, SP, Brazil*

<sup>3</sup>*Instituto de Física, Universidade Federal de Uberlândia, 38400-902, Uberlândia, MG, Brazil*

<sup>4</sup>*Departamento de Física, Universidad Técnica Federico Santa María, Casilla 110-V, Valparaíso, Chile*

(Dated: June 30, 2025)

This study theoretically investigates the contact conductance in twisted bilayer graphene (TBG), providing a theoretical explanation for recent experimental observations from scanning tunneling microscopy (STM) and conductive atomic force microscopy (c-AFM). These experiments revealed a surprising non-monotonic current pattern as a function of the TBG rotation angle  $\theta$ , with a peak at  $\theta \approx 5^\circ$ , a finding that markedly departs from the well-known magic angle TBG behavior. To elucidate this phenomenon, we develop a comprehensive theoretical and computational framework. Our calculations, performed on both relaxed and rigid TBG structures, simulate contact conductance by analyzing the local density of states across a range of biases and rotational angles. Contrary to the current interpretation, our results demonstrate that the maximum conductance at  $\theta \approx 5^\circ$  is not caused by structural relaxation or AA stacking zone changes. Instead, we attribute this peak to the evolution of the electronic band structure, specifically the shifting of van Hove singularities (vHs) to the Fermi level as the twist angle decreases. We further show that the precise location of this conductance maximum is dependent on the applied bias voltage. This interplay between twist angle, bias, and vHs energy provides a robust explanation for the experimental findings.

## I. INTRODUCTION

Twisted bilayer graphene (TBG) systems offer a new platform for exploring emergent quantum phenomena in condensed matter[1]. By controlling the twist angle between two graphene layers, one can induce a periodic moiré superlattice that dramatically alters the electronic band structure [2]. At specific “magic angles”, flat bands appear near the Fermi level [3–5], enhancing electron-electron interactions and enabling the formation of correlated insulating and superconducting phases [6–8]. These findings have spurred significant interest in understanding the intricate interplay between topology and interactions in TBG systems.

Important insights on the properties of TBG systems can be obtained from scanning probe microscopy (STM) [9–11] and standard and conductive atomic force microscopy (c-AFM) [12–17]. By measuring the contact conductivity of TBG systems as a function of the twist angle  $\theta$ , these techniques provide valuable quantitative information on the system’s local density of states (LDOS) and lattice relaxation.

Bistritzer and MacDonald predicted six interlayer conductivity peaks in twisted few-layer graphene at specific twist angles, including  $\theta = 21.8^\circ$  and  $38.2^\circ$  [18]. Experimental evidence supporting these predictions was provided by two independent groups [12, 13] using conductive Atomic Force Microscopy (c-AFM). These studies observed enhanced interlayer conductivity at the aforementioned angles in graphite-based systems. While these findings partially validate the theoretical predictions, the absence of the other four predicted peaks remained a puzzle.

Early experimental work [19] demonstrated that incommensurate interfaces, lacking Fermi surface overlap, suppress interlayer coupling and conductivity. Subsequent studies experimentally investigated the dependence of the interlayer conductivity on twist-angle  $\theta$  in TBG systems [15, 16] and even in other Van der Waals materials, such as MoS<sub>2</sub>/graphene heterostructures [14]. Ref. [15] did not observe an exceptionally enhanced conductivity at the angles predicted by theory [18] and found a linear dependence on the  $\theta$  for large twist-angles, consistent with the theoretical prediction based on a phonon-mediated interlayer transport mechanism, considering the renormalization of the Fermi velocity [20]. Zhang and collaborators [16] reported a maximum in interlayer conductivity around  $\theta \approx 5^\circ$  followed by a decrease in larger twist-angle TBG samples. This behavior was attributed to the increasing dominance of low-conductivity AB-stacked regions in the moiré pattern. However, their interpretation based on *ab initio* carrier density may not be entirely accurate, as the energy window used for integration is somewhat too large to directly correlate with STM measurements. Despite significant progress, a comprehensive understanding of vertical transport mechanisms in bilayer or few-layer two-dimensional (2D) electronic systems remains elusive [14–16].

In this study, we investigate the contact conductance in TBG systems, specifically addressing recent experimental observations from scanning tunneling microscopy (STM). Our approach involves simulating the system’s lattice reconstruction and computing its local density of states (LDOS). Contrary to previous predictions, our findings reveal that the experimentally observed maximum in local conductance at  $\theta \approx 5^\circ$  is not a consequence of struc-

tural relaxation. Instead, we demonstrate that this peak is directly linked to the evolution of the electronic band structure as a function of the twist angle, particularly the shifting of van Hove singularities (vHs) to the Fermi level. Furthermore, we show that the contact conductance remains practically the same for both relaxed and rigid TBG systems at a given twist angle.

This paper is organized as follows. In Sec. II, we discuss the description of TBG crystal structures as a function of the twist angle  $\theta$ , including their symmetries, and outline our approach for computing lattice relaxation effects. We also introduce an efficient methodology to estimate the size of the AA-stacking region. Next, we present the effective tight-binding Hamiltonian employed to calculate the low-energy electronic properties of TBGs and detail our simulation approach for STM measurements. In Sec. III, we quantify the in-plane and out-of-plane lattice relaxation effects as a function of the twist angle  $\theta$  and compare the LDOS for each case. Later, we show how the peak in the local conductance depends on the relative rotational angle and on the STM bias. We discuss our results and present our conclusions in Sec. IV.

## II. THEORY AND METHODS

### A. Structural calculations

TBG lattices are characterized, as standard [2, 21], by the twist of one graphene layer with respect to the other around a given site starting from the AB-stacked bilayer, forming a moiré pattern. We take the primitive lattice vectors of the bottom layer as  $\mathbf{a}_1^b = \sqrt{3}a_0/2 (\sqrt{3}\hat{e}_x + \hat{e}_y)$  and  $\mathbf{a}_2^b = \sqrt{3}a_0/2 (\sqrt{3}\hat{e}_x - \hat{e}_y)$  and those of top layer as  $\mathbf{a}_i^t = R(\theta)\mathbf{a}_i^b$ , where  $R(\theta)$  is the rotation matrix. For non-relaxed TBGs lattices, we set the graphene carbon-carbon bond length as  $a_0 = 1.42 \text{ \AA}$  (with corresponding single-layer lattice constant  $a = \sqrt{3}a_0$ ), and the spacing between graphene layers as  $d_0 = 3.35 \text{ \AA}$  [4].

The lattice structure of a TBG system is periodic if the periods of the two graphene layers match, giving a finite unit cell. Hence, the periodicity condition requires the lattice translation vector  $m\mathbf{a}_1^b + n\mathbf{a}_2^b$  of the bottom (unrotated) layer and  $n\mathbf{a}_1^t + m\mathbf{a}_2^t$  in the top (rotated) layer, with  $m$  and  $n$  integers, to coincide. The twist angle for a commensurate structure is related to  $(m, n)$  by [22–24]

$$\theta(m, n) = \arccos\left(\frac{1}{2} \frac{m^2 + n^2 + 4mn}{m^2 + n^2 + mn}\right), \quad (1)$$

with a lattice constant

$$L = a_0 \sqrt{3(m^2 + n^2 + mn)} = \frac{|m - n|\sqrt{3}a_0}{2 \sin \theta/2}, \quad (2)$$

which contains  $N = 4(m^2 + n^2 + mn)$  atoms.

Each graphene layer comprises two sublattices, denoted as  $A^{b(\text{or } t)}$  and  $B^{b(\text{or } t)}$ . Commensurate structures

occur in two distinct forms identified by their sublattice parities [23–25]. Figure 1 shows an example of an odd commensurate structure, which is characterized by having 3 three-fold symmetric positions, corresponding to the stacking of  $B^b H^t$ ,  $A^b A^t$  and  $H^b B^t$  sites, indicated by star points. We label by  $B^b H^t$  (or  $H^b B^t$ ) the sites where a  $B^b$  (or  $B^t$ )-sublattice site of one layer aligns with the hexagonal centers  $H^t$  (or  $H^b$ ) of its neighboring layer. We chose to investigate odd commensurate structures for convenience, but the parity of the system does not affect our findings.

To facilitate the analysis of TBG lattice structures and efficiently identify all distinct equivalent sites within a unit cell, let us examine their symmetries. In Fig. 1, the carbon atom sites marked by identical colored disks are equivalent due to their  $C_3$  three-fold symmetric positions. A practical approach to select the nonequivalent atomic sites is to connect (blue lines) the points of two  $A^b A^t$  sites and one  $B^b H^t$  (or  $H^b B^t$ ) site. These lines form a triangular area encompassing one-sixth of the unit cell's total area. Notably, the blue lines connecting two  $A^b A^t$  sites correspond to the  $C_2'$  two-fold rotation axes, providing a clear and efficient means to distinguish between all different equivalent sites within the unit cell.

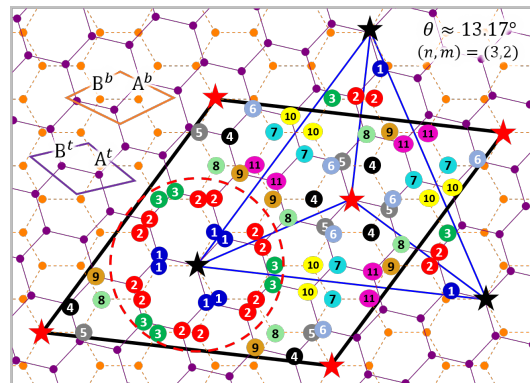


FIG. 1. TBG commensurate structure with  $\theta \approx 13.17^\circ$  that corresponds to  $(m, n) = (3, 2)$ . Purple (orange) circles and lines indicate the carbon sites and the primitive unit cell of the top (bottom) layer, respectively. The black lines outline the primitive unit cell of the TBG system. Black (red) stars indicate the  $A^b A^t$  ( $B^b H^t$  or  $H^b B^t$ ) sites. Sites labeled by the same number (same color) are equivalent. The dashed red circle outlines the AA-stacking region.

Starting from the above-defined lattice structures, we determine the atomic relaxation positions for a given twist-angle  $\theta$  using the Large-scale Atomic/Molecular Massively Parallel Simulator (LAMMPS) [26]. The energy minimization process incorporates both non-bonded and bonded interactions to model the system accurately. Non-bonded interlayer interactions are handled using a registry-dependent interlayer potential specifically designed for graphene/hBN heterostructures [27–29], with a cutoff distance of  $16 \text{ \AA}$ , ensuring that all relevant interlayer forces are considered. The parameters for the

registry-dependent potential are given in [30]. Bonded intralayer interactions within each layer are modeled using the Tersoff potential [31, 32], which is well-suited for describing the covalent bonding in carbon-based materials like graphene. The lattice structure relaxation calculations are performed with an energy tolerance criterion set to  $10^{-10}$  eV per atom [33], ensuring high precision in determining the equilibrium atomic positions.

## B. Evaluation of the AA-stacking region area

In rigid lattice structures, the area of the AA-stacking region encompasses a set of equivalent and equidistant sites relative to an  $A^bA^t$  site. As shown in Fig. 1, for a twist angle of  $\theta \approx 13.17^\circ$ , only sites 1, 2, and 3 (depicted as blue, red, and green disks) are both equivalent and equidistant from the central “black star” lattice site. The radius of the AA-region area,  $r_{AA}^{\text{rig}} \approx 2.85$  Å, is defined by the furthest of these equivalent sites within the AA zone. Notably, these sites belong to different layers, which are vertically aligned when  $\theta = 0$ . We denote their distance as  $d_c$ . Conversely, the equidistant sites relative to a  $B^bH^t$  (or  $H^bB^t$ ) site of the AB-stacking region are not equivalent. This is evident in Fig. 1 by examining sites 4, 5 and 6 (depicted by black, gray and light blue disks, respectively). Each of these sites belongs to a different symmetry group within the AB zone to the due varying graphene layer alignments.

Figure 2 provides a schematic representation of the lattice structure within the AA-stacking region. In relaxed lattice structures, we observe a distinctive pattern in the atomic position displacement vectors. Specifically, the  $xy$ -plane projections of the atomic position displacement vectors,  $\Delta\mathbf{R}_i(x, y) = \mathbf{R}_i^{\text{relaxed}} - \mathbf{R}_i^{\text{rigid}}$  [indicated by the black arrows in Fig. 2(c)] are perpendicular to the radial vectors originating from the central  $A^bA^t$  site. Moreover, their angular components exhibit opposite directions in the two graphene layers within the AA zone. Furthermore, the magnitudes of the displacement vectors  $\Delta\mathbf{R}_i(x, y)$  increase linearly with the radial distance from the central  $A^bA^t$  site.

The area of the AA-stacking region in a relaxed lattice structure for a given twist angle is evaluated similarly to the rigid lattice case, but with an additional constraint: The distance between two furthest equivalent atomic sites belonging to different layers must remain within the upper bound,  $d_c$ , established for the rigid lattice structure at the same twist angle  $\theta$ . This is visually represented by the blue arrow in Figs. 2(b) and (c). The atomic displacement distances, represented by green arrows in Fig. 2(c), increase due to lattice relaxation. Consequently, owing to the constraint imposed by  $d_c$ , the relaxed TBG lattice structures exhibit a smaller AA-stacking region area compared to their rigid counterparts, as illustrated by Fig. 2(d).

In summary, we propose a novel and simple method to determine the AA-stacking area based on the anal-

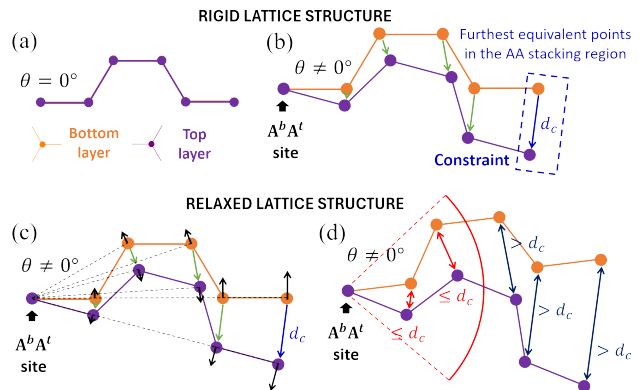


FIG. 2. Schematic representation of the lattice structure in the AA-stacking region. Purple (orange) circles indicate the carbon sites of the top (bottom) layer. The green arrows correspond to the displacement vectors due to the twist angle. The blue arrow represents the constraint that defines the AA-region area. (a) Rigid lattice with  $\theta = 0$ . (b) Rigid lattice structure with  $\theta \neq 0$ . (c) and (d) Relaxed lattice structure for  $\theta \neq 0$ . The black arrows correspond to displacement vectors due to relaxation. The dashed lines indicate the radial distances with respect to site  $A^bA^t$ . The dashed and solid red lines correspond to the circular sector of the AA-region area.

ysis of local symmetry regions. This approach offers a clear advantage over the method presented in Ref. [16], which relies on averaged values obtained from a range of arbitrary cut-off distances.

## C. Electronic calculations

The low-energy electronic properties of TGBs are obtained using a tight-binding model following Nam and Koshino [34]:

$$H = - \sum_{i,j} t(\mathbf{R}_i - \mathbf{R}_j) |\mathbf{R}_i\rangle \langle \mathbf{R}_j| + \text{H.c.}, \quad (3)$$

where  $\mathbf{R}_i$  is the position of the  $i$ th atom and  $\langle \mathbf{r} | \mathbf{R}_i \rangle$  is the corresponding  $p_z$  orbital wave function. The transfer integral  $t(\mathbf{R})$  depends on the interatomic distance and the relative orientation between  $p_z$  orbitals connected by  $\mathbf{R}$ . The transfer integral is parametrized as

$$-t(\mathbf{R}) = V_{pp\pi}(R) \left[ 1 - \left( \frac{\mathbf{R} \cdot \mathbf{e}_z}{R} \right)^2 \right] + V_{pp\sigma}(R) \left( \frac{\mathbf{R} \cdot \mathbf{e}_z}{R} \right)^2, \quad (4)$$

where the hopping parameters  $V_{pp\pi}(R)$  and  $V_{pp\sigma}(R)$  are given by

$$V_{pp\pi}(R) = V_{pp\pi}^0 \exp\left(-\frac{R-a_0}{r_0}\right) \quad (5)$$

$$V_{pp\sigma}(R) = V_{pp\sigma}^0 \exp\left(-\frac{R-d_0}{r_0}\right), \quad (6)$$

with  $V_{pp\pi}^0 = -2.65$  eV and  $V_{pp\sigma}^0 = 0.48$  eV, whereas  $r_0 = 0.184a$  is the hopping matrix element decay length.

The electronic local density of states (LDOS),  $\rho(\mathbf{r}, \varepsilon)$ , of the TBG systems under investigation is computed by direct diagonalization and by the HHK recursive technique [25, 35, 36].

#### D. Modeling STM measurements

We estimate the local conductance using the Bardeen's theory [37–39] and Tersoff-Hamann formula [38, 40, 41], with a combination of direct diagonalization and the Haydock-Heine-Kelly (HHK) recursive technique, considering lattice relaxations obtained from semi-empirical forces.

At low temperatures, the STM current is given by [37–39]

$$I(\mathbf{r}) = \frac{4\pi e}{\hbar} \int_0^{eV} d\varepsilon \rho_S(\mathbf{r}, \varepsilon_F - eV - \varepsilon) \rho_T(\varepsilon_F + \varepsilon) |M|^2 \quad (7)$$

where  $V$  is the sample-tip bias voltage,  $\rho_S$  stands for the surface LDOS,  $\rho_T$  for tip LDOS, and  $M$  is the electron tip-surface tunneling transition matrix element. Assuming that the LDOS tip has a very smooth energy dependence, the tunneling current can be approximated as [39]

$$I(\mathbf{r}) \propto \left[ \int_0^{eV} \rho_S(\mathbf{r}, \varepsilon) d\varepsilon \right] e^{-h(\mathbf{r})\kappa(\mathbf{r})}, \quad (8)$$

where the inverse decay length  $\kappa \sim \sqrt{2m\phi/\hbar}$  is determined by the local barrier height or average work function. The exponential dependence on tip-sample distance  $h(\mathbf{r})$  makes it possible to obtain high-resolution surface topography at a given bias voltage. An STM image not only reflects topography but also contains information about the sample LDOS, which can be obtained directly [39, 42] by measuring the local differential conductance

$$\frac{dI(\mathbf{r})}{dV} \propto \rho_S(\mathbf{r}, \varepsilon = eV), \quad (9)$$

where for simplicity  $\varepsilon_F$  has been set to be zero. The calculated local differential conductance, as described above, is a key quantity in this study, since it allows for a direct comparison with STS measurements, as reported in Refs. [14–16].

Lattice relaxation modifies  $\rho_S(\mathbf{r}, \varepsilon_F)$ , causing, for instance, the shrinking of the AA-stacking region. Out-of-plane relaxation also affects  $|M|^2$ , which depends exponentially on the tip-surface distance.

Our STM simulations are conducted for the constant height mode. We model the LDOS of a given site as a  $p_z$  orbital centered on the atomic positions, considering only the contribution from the two highest valence bands. This is equivalent to sweeping a range of states with energies 100 meV below the Fermi level. As shown

below, a 100 meV gate effectively captures the salient features of the LDOS within the AA region of the unit cell. The magnitude of the STM current at a specific point of the surface map is obtained by summing the calculated LDOS contribution from all atomic positions, accounting for the exponential decay of the tunneling current with distance.

### III. RESULTS

#### A. Structural relaxation

We will now focus on examining the out- and in-plane relaxation of TBG lattice structures, obtained by the LAMMPS simulations. Here, we consider the  $|n-m| = 1$  family of odd commensurate lattice structures.

##### 1. Out-of-plane relaxation

We quantify the out-of-plane relaxation by the average vertical displacement defined as

$$\Delta\bar{\mathbf{z}}_i = \frac{1}{M} \sum_{j=1}^M (\mathbf{z}_{i,\text{top}}^{\text{relaxed}} - \mathbf{z}_{j,\text{bottom}}^{\text{relaxed}} - \mathbf{d}_0), \quad (10)$$

where for each atomic site  $i$  of the top layer, the average considers the set of atoms  $j$  of the bottom layer within a circular radius of 5 Å centered on  $i$ , with  $\mathbf{d}_0 = d_0\hat{\mathbf{e}}_z$ .

Figure 3 presents contour plots illustrating the out-of-plane average displacement  $\Delta\bar{\mathbf{z}}_i$  within the moiré unit cell of TBGs with  $\theta \approx 2.45^\circ$ ,  $1.29^\circ$ ,  $1.12^\circ$  and  $0.59^\circ$ , encompassing 2188, 7804, 10444 and 38308 carbon atoms, respectively. The bright areas ( $\Delta\bar{\mathbf{z}}_i > 0$ ) correspond to atomic sites with the largest out-of-plane displacements following lattice structural relaxation. These areas coincide with the AA-stacking regions, specifically at one-third of the largest diagonal of the unit cell. Conversely, the dark areas ( $\Delta\bar{\mathbf{z}}_i < 0$ ) correspond to the AB-stacking regions located at the vertices of the unit cell and at two-thirds of its larger diagonal.

To highlight the atomic sites with the most prominent enhancement of out-of-plane displacement in TBGs, we consider the  $A^bA^t$  and  $H^bB^t$  (or  $B^bH^t$ ) sites as representative sites of the AA- and AB-stacking regions, respectively. Figures 4(a) and (b) illustrate the evolution of the out-of-plane displacement, twist angle  $\theta$  at the  $A^bA^t$  and  $H^bB^t$  atomic sites, respectively.

As shown in Fig. 4(a), a decrease in twist angle leads to a significant increase in the out-of-plane displacement vectors of the AA-stacking region ( $\bar{\mathbf{z}}_{AA} > 0$ ). The maximum displacement of  $\sim 0.15$  Å occurs at a twist angle of  $\theta \approx 5^\circ$ , corresponding to  $(m, n) = (6, 7)$  with 508 carbon atoms within the moiré cell. This indicates that the AA-stacking region is further apart by  $\sim 0.30$  Å, relative to the spacing  $d_0$  of a non-relaxed lattice. In contrast, the AB-stacking regions exhibit an interlayer

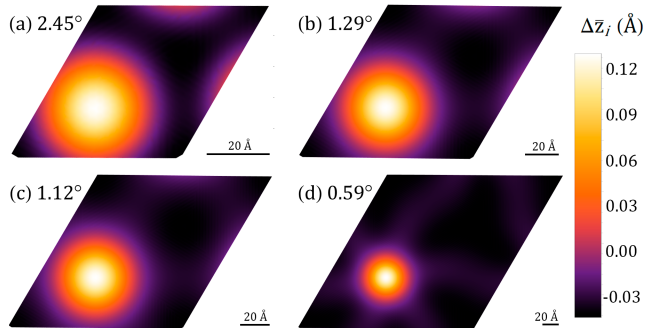


FIG. 3. Spatial representation of the average out-of-plane displacement  $\Delta\bar{z}_i$  within of the moiré unit cell for the twist angles (a)  $\theta \approx 2.45^\circ$ , (b)  $1.29^\circ$ , (c)  $1.12^\circ$ , and (d)  $0.59^\circ$ . The color scale bar indicates the values of  $\Delta\bar{z}_i$  (in angstrom).

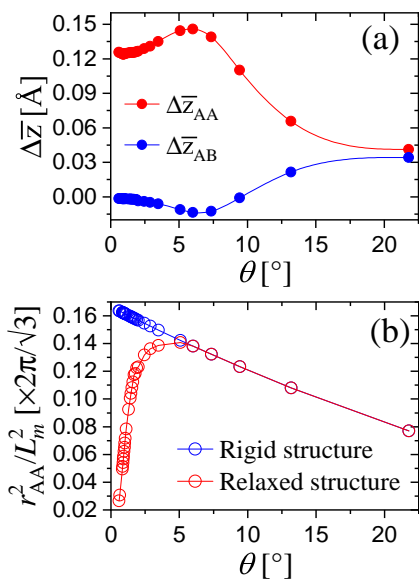


FIG. 4. (a) Out-of-plane displacement vectors  $\Delta\bar{z}_{AA}$  and  $\Delta\bar{z}_{AB}$  (in angstrom) at the  $A^bA^t$  and  $H^bB^t$  atomic sites, respectively, of the top layer as a function of twist angle  $\theta$  (in degrees). (b) The ratio between the AA-region area and the area of the moiré unit cell,  $\propto r_{AA}^2/L_m^2$ , as a function of  $\theta$  (in degrees). The blue and red open points correspond to the rigid and relaxed lattice structure, respectively.

spacing that exceeds  $d_0$  ( $\bar{z}_{AB} > 0$ ) for  $\theta > 10^\circ$ . However, for  $\theta < 10^\circ$  the graphene layers in the AB-stacking are brought closer together, with a spacing smaller than  $d_0$  ( $\bar{z}_{AB} < 0$ ). The minimum displacement of  $\sim 0.014$  Å occurs close to  $\theta = 5^\circ$ , indicating that the AB-stacking regions are closer by  $\sim 0.028$  Å.

## 2. In-plane relaxation

We can evaluate the horizontal stress of the lattice by calculating the differences between the atomic positions

in the rigid and relaxed structures. The in-plane displacement vectors  $\Delta\mathbf{R}_i(x, y) = \mathbf{R}_i^{\text{relaxed}} - \mathbf{R}_i^{\text{rigid}}$  reach a maximum at the boundary of the AA-stacking region, which assumes a circular shape. Our calculations indicate that the carbon-carbon nearest neighbor bond modifications are negligible for  $\theta \gtrsim 5^\circ$ . However, as the twist angle decreases below  $\theta \lesssim 5^\circ$ , the carbon-carbon nearest neighbor bond modifications increase significantly. Carbon atoms are increasingly displaced to restore AB- and BA-stacking, which assumes triangular domains.

Let us now examine the AA-region area of the rigid and relaxed lattice structures using the procedure described in Sec. II B based on point group symmetries. Figure 4(b) presents the ratio between the AA-region area, proportional to  $r_{AA}^2$ , and the area of the moiré cell, proportional to  $L_m^2$ , as a function of twist angle  $\theta$  for both rigid and relaxed lattice structures. Given the  $1/\theta^2$  dependence of the moiré cell area at small twist angles, see Eq. (2), the ratio  $r_{AA}^2/L_m^2$  exhibits a linear dependence for rigid lattice structures. However, the calculations show a clear deviation from this linear behavior for  $\theta < 5^\circ$  upon lattice relaxation. This deviation indicates a significant reduction in the AA-region area within moiré unit cells with  $\theta < 5^\circ$ , as further corroborated by Fig. 3. Consequently, the triangular domains of the AB- and BA-stacking regions expand.

In summary, in the absence of lattice relaxation, a decrease in twist angle inherently leads to an increase in AA-stacking region size. However, given that AA stacking is energetically less favorable than AB stacking, the system undergoes lattice relaxation to minimize these high-energy areas. This minimization involves in-plane relaxation, which contracts AA regions by pulling edge atoms towards the more stable AB configuration, consequently expanding the AB and BA domains. Simultaneously, out-of-plane relaxation causes an increased interlayer separation within AA regions, thereby relieving the associated strain. The  $5^\circ$  twist angle represents a critical point where the system balances the competing effects of minimizing AA area and accommodating the associated strain through a combination of out-of-plane and in-plane relaxations. This balance is reflected in the maximum interlayer separation observed in AA regions and the minimum separation in AB regions around this angle.

This represents the prevailing and appealing explanation for the contact conductance peak at a  $\theta = 5^\circ$  twist angle. However, through a careful analysis of the LDOS and detailed modeling of STM measurements, we demonstrate in the following that this is not the dominant mechanism responsible for the observed peak.

## B. Analysis of STM in constant height mode

We now apply the theoretical framework and methods outlined in Sections II to analyze the vertical current reported in the STM experiment [16].

We begin by examining the impact of in-plane relaxation on contact conductance. Figures 5(a) to (d) present mappings of the LDOS obtained by STM simulations with constant height mode at 1 Å from the surface, based on the tight-binding model given by Eq. (3). These simulations are performed for twisted angles of 5.09° and 1.12°, considering both rigid [panels (a) and (b)] and relaxed crystalline structures [panels (c) and (d)]. For  $\theta \approx 5.09^\circ$ ,  $3 \times 3$  superstructures are plotted in Fig. 5(a) and (c). The shrinking of the AA-stacking regions [bright zones in Fig. 5 (a)-(d)] is evident when comparing both relaxed and rigid configurations across all panels, and the STM simulations are consistent with the experimental findings [16]. This reduction underscores the significant impact of in-plane lattice relaxation, which tends to suppress AA-stacking areas due to its inherent instability, as discussed in Sec. II A.

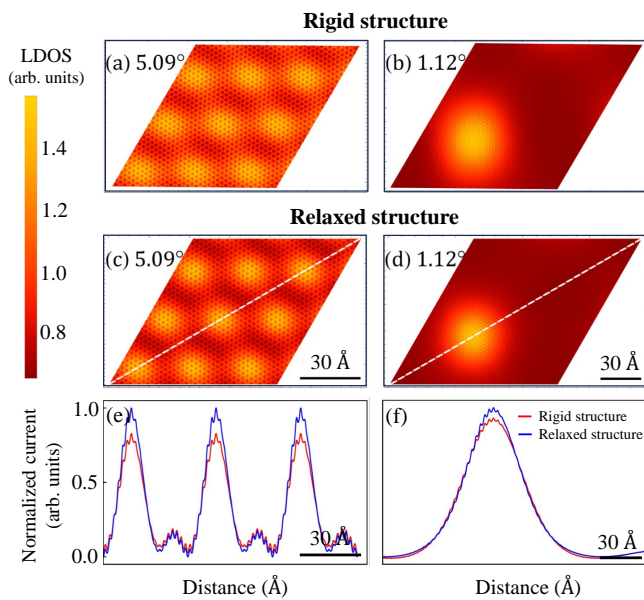


FIG. 5. STM simulations in constant height mode for  $\theta \approx 5.09^\circ$  and  $1.12^\circ$ . Panels (a) and (b) show LDOS (in arbitrary units) for rigid structures, while (c) and (d) for relaxed ones. The white dashed lines in panels (c) and (d) indicate the paths along which the normalized current profiles are calculated. Panels (e) and (f) show the normalized current (in arbitrary units) along the path for the relaxed structures at  $\theta \approx 5.09^\circ$  and  $1.12^\circ$ , respectively. The simulations consider the states belonging to the two highest valence bands for each structure.

Furthermore, we simulate the current (or contact conductance) profile as the tip moves along the main diagonal of the unit cell. Figures 5(e) and (f) display the normalized current measured along the main diagonal [white dashed lines in Fig. 5(c) and (d)] of the unit cell for  $\theta \approx 5.09^\circ$  and  $1.12^\circ$ , respectively. The reported currents are normalized to a maximum value of 1 in arbitrary units. The highest normalized current value is obtained around the AA-stacking region, consistent with the enhanced LDOS in these areas, which amplifies the vertical

current. Conversely, regions with low normalized current correspond to AB- and BA-stacking regions.

We highlight two important aspects concerning the current in the AA region. Firstly, the current for the relaxed structure at the AA region is roughly 10% larger than that for the rigid one, as illustrated by Figs. 5(e) and (f). This can be understood by considering that relaxation compresses the AA region, and thus the states within the energy range between the Fermi level and the tip bias value become confined to a reduced area, increasing the current. As previously noted, the current calculation includes contributions from all atoms on the surface. More importantly, given that the current is calculated in constant height mode, and considering our prior finding that the AA zone slightly protrudes out of the plane in the relaxed structure, this out-of-plane displacement further enhances the observed current. Secondly, while one might naively expect a broadening of the peak for the rigid structure, and that is not observed. We attribute this to our current calculation methodology, which considers the contribution of all surface atoms, not merely those directly beneath the tip.

It is important to note that only surface atoms are explicitly considered in the current calculation, since the contribution from the lower layer is deemed negligible due to the exponential decay of electron wave functions. The influence of the lower layer is implicitly accounted for in the wave function of the surface atoms, similar to observations in graphite or bilayer graphene with a triangular lattice[43]

### C. Vertical transport, contact conductance and local density of states.

We now proceed to fully analyze the maximum in the contact conductance observed at 5° and elucidate its origin. For each twist angle  $\theta$  and for both rigid and relaxed structures, we calculate the current at 1 Å above the AA site with respect to the mean value of the  $z$ -coordinate of the top layer. The current at this position is proportional to the integral of the LDOS from  $-V_{\text{bias}}$  up to the Fermi level (as given by the integral within the bracket of Eq. (8)).

Figure 6(a) shows the local carrier density at the AA site as a function of the twist angle  $\theta$  for rigid and relaxed structures across three bias voltages  $-V_{\text{bias}}$ : 100, 300, and 500 meV. We observe a clear maximum in the current that is angle-dependent, with its precise position shifting with  $V_{\text{bias}}$ . Notably, the position of the maximum is consistent for both rigid and the relaxed structures. Specifically, the maximum is located at  $\theta \approx 7^\circ$  for  $V_{\text{bias}} = 500$  meV,  $\theta \approx 5^\circ$  for  $V_{\text{bias}} = 300$  meV, and  $\theta \approx 2^\circ$ , for  $V_{\text{bias}} = 100$  meV.

To understand this behavior, we present the LDOS at the AA site for three selected angles, for both relaxed and rigid structures, in Figs. 6(c)-(d). For each plot, the highlighted regions indicate the energy range for the contact

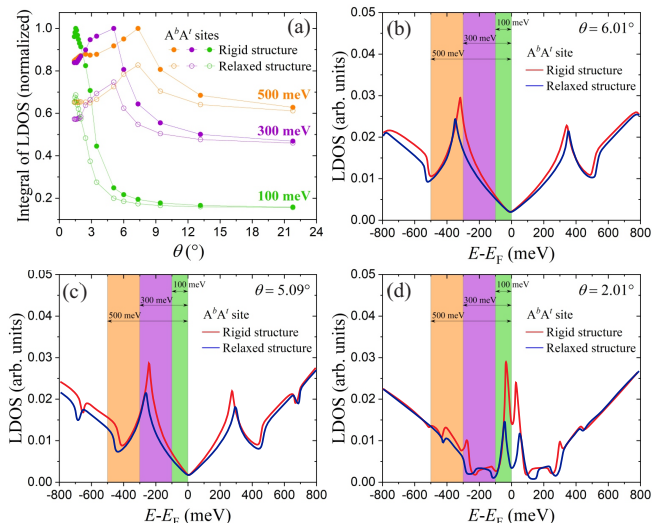


FIG. 6. Local density of states at the  $A^b A^t$  atomic sites for three twist angles: (a)  $6.01^\circ$ , (a)  $5.09^\circ$  and (c)  $2.01^\circ$ . The shadowed regions from the Fermi level up to 100, 300, and 500 meV are used to calculate the integral proportional to the current measured by an STS tip. The potential difference between the tip and the surface equals these values.

conductance calculation. While the LDOS of the two structure types (rigid and relaxed) differs only slightly, the position of the maximum current is directly related to the location of the van Hove singularities (vHs) and whether they fall within the energy range between  $V_{\text{bias}}$  and the Fermi level. Specifically, for  $6^\circ$  the vHs falls within the integration range only from  $V_{\text{bias}} = -500$  meV case. Conversely, for  $V_{\text{bias}} = -300$  meV the vHs enters this integration range only for angles less than  $5^\circ$ .

These findings definitively rule out the explanation that the position of this maximum is related to the relaxation of the structure and the relative increase of the AA zone, which peaks at  $\theta \approx 5^\circ$  [16].

It is worth noting that the carrier density at  $H^b B^t$  site as a function of the angle, exhibits a similar trend to that at  $A^b A^t$  site, but with reduced intensity. All results presented in this section have been obtained using both direct diagonalization and the HHK recursive technique [25, 35, 36], considering both relaxed and rigid lattice structures.

#### IV. CONCLUSIONS AND DISCUSSION

In this study, we investigate the intriguing behavior of contact conductance in TBG systems, providing a robust

theoretical framework to explain recent, unexpected experimental observations from STM and *c*-AFM. These experiments highlighted a surprising non-monotonic current pattern dependent on the TBG rotation angle  $\theta$ , with a prominent peak around  $\theta = 5^\circ$ . This finding presented a significant departure from the widely recognized magic angle behavior of TBG, prompting our comprehensive investigation.

Our theoretical and computational approach, applied to both relaxed and rigid TBG structures, allowed us to simulate contact conductance by systematically analyzing the LDOS across various biases and rotational angles. A key insight from our work is the invalidation of the current interpretation that links the observed conductance maximum to structural relaxation or changes in the AA-stacking area. While structural relaxation indeed plays a crucial role in modifying the physical dimensions of stacking regions, our simulations conclusively demonstrated that it is not the primary driver for the conductance peak at  $\theta = 5^\circ$ . Instead, our findings firmly establish that the conductance maximum directly originates from the evolution of the electronic band structure. Specifically, we identified the shifting of van Hove singularities (vHs) toward the Fermi level as the underlying mechanism as the twist angle decreases. This energetic alignment of vHs with the Fermi level has a profound impact on the available electronic states for tunneling, leading to the observed conductance enhancement.

Furthermore, we revealed a critical dependence of the conductance maximum's precise location on the applied bias voltage. This interplay between twist angle, bias voltage, and the energy of the vHs provides a comprehensive and compelling explanation for the experimental observations. Our results not only clarify the previously puzzling experimental data but also reveal the profound influence of subtle electronic band structure dynamics on the macroscopic transport properties of TBG. This understanding is crucial for designing and optimizing future graphene-based electronic devices, particularly those that rely on tunable contact properties.

#### ACKNOWLEDGMENTS

This work was supported by the Brazilian funding agencies CNPq, CAPES, FAPERJ, FAPESP, and FAPEMIG. ESM acknowledges financial support from ANID project 1221301.

- 
- [1] E. Y. Andrei and A. H. MacDonald, Graphene bilayers with a twist, *Nat. Mater.* **19**, 1265 (2020).  
 [2] J. Lopes dos Santos, N. Peres, and A. C. Neto, Graphene

- bilayer with a twist: Electronic structure, *Phys. Rev. Lett.* **99**, 256802 (2007).  
 [3] E. Suárez Morell, J. D. Correa, P. Vargas, M. Pacheco,

- and Z. Barticevic, Flat bands in slightly twisted bilayer graphene: Tight-binding calculations, *Phys. Rev. B* **82**, 121407 (2010).
- [4] G. Trambly de Laissardière, D. Mayou, and L. Magaud, Localization of Dirac electrons in rotated graphene bilayers, *Nano Lett.* **10**, 804 (2010).
- [5] R. Bistritzer and A. H. MacDonald, Moiré bands in twisted double-layer graphene, *Proc. Natl. Acad. Sci. U.S.A.* **108**, 12233 (2011).
- [6] Y. Cao, V. Fatemi, S. Fang, K. Watanabe, T. Taniguchi, E. Kaxiras, and P. Jarillo-Herrero, Unconventional superconductivity in magic-angle graphene superlattices, *Nature* **556**, 43 (2018).
- [7] Y. Cao, V. Fatemi, A. Demir, S. Fang, S. L. Tomarken, J. Y. Luo, J. D. Sanchez-Yamagishi, K. Watanabe, T. Taniguchi, E. Kaxiras, R. C. Ashoori, and P. Jarillo-Herrero, Correlated insulator behaviour at half-filling in magic-angle graphene superlattices, *Nature* **556**, 80 (2018).
- [8] M. Yankowitz, S. Chen, H. Polshyn, Y. Zhang, K. Watanabe, T. Taniguchi, D. Graf, A. F. Young, and C. R. Dean, Tuning superconductivity in twisted bilayer graphene, *Science* **363**, 1059 (2019).
- [9] D. Wong, Y. Wang, J. Jung, S. Pezzini, A. M. DaSilva, H.-Z. Tsai, H. S. Jung, R. Khajeh, Y. Kim, J. Lee, S. Kahn, S. Tollabimazraehno, H. Rasool, K. Watanabe, T. Taniguchi, A. Zettl, S. Adam, A. H. MacDonald, and M. F. Crommie, Local spectroscopy of moiré-induced electronic structure in gate-tunable twisted bilayer graphene, *Phys. Rev. B* **92**, 155409 (2015).
- [10] N. Tilak, X. Lai, S. Wu, Z. Zhang, M. Xu, R. de Almeida Ribeiro, P. C. Canfield, and E. Y. Andrei, Flat band carrier confinement in magic-angle twisted bilayer graphene, *Nat. Commun.* **12**, 4180 (2021).
- [11] D. Călugăru, N. Regnault, M. Oh, K. P. Nuckolls, D. Wong, R. L. Lee, A. Yazdani, O. Vafek, and B. A. Bernevig, Spectroscopy of twisted bilayer graphene correlated insulators, *Phys. Rev. Lett.* **129**, 117602 (2022).
- [12] E. Koren, I. Leven, E. Lörtscher, A. Knoll, O. Hod, and U. Duerig, Coherent commensurate electronic states at the interface between misoriented graphene layers, *Nat. Nanotech.* **11**, 752 (2016).
- [13] T. Chari, R. Ribeiro-Palau, C. R. Dean, and K. Shepard, Resistivity of rotated graphite-graphene contacts, *Nano Lett.* **16**, 4477 (2016).
- [14] M. Liao, Z.-W. Wu, L. Du, T. Zhang, Z. Wei, J. Zhu, H. Yu, J. Tang, L. Gu, Y. Xing, R. Yang, D. Shi, Y. Yao, and G. Zhang, Twist angle-dependent conductivities across MoS<sub>2</sub>/graphene heterojunctions, *Nat. Commun.* **9**, 4068 (2018).
- [15] Z. Yu, A. Song, L. Sun, Y. Li, L. Gao, H. Peng, T. Ma, Z. Liu, and J. Luo, Understanding interlayer contact conductance in twisted bilayer graphene, *Small* **16**, 1902844 (2020).
- [16] S. Zhang, A. Song, L. Chen, C. Jiang, C. Chen, L. Gao, Y. Hou, L. Liu, T. Ma, H. Wang, X.-Q. Feng, and Q. Li, Abnormal conductivity in low-angle twisted bilayer graphene, *Sci. Adv.* **6**, eabc5555 (2020).
- [17] X. Huang, L. Chen, S. Tang, C. Jiang, C. Chen, H. Wang, Z.-X. Shen, H. Wang, and Y.-T. Cui, Imaging dual-moiré lattices in twisted bilayer graphene aligned on hexagonal boron nitride using microwave impedance microscopy, *Nano Lett.* **21**, 4292 (2021).
- [18] R. Bistritzer and A. H. MacDonald, Transport between twisted graphene layers, *Phys. Rev. B* **81**, 245412 (2010).
- [19] Y. Kim, H. Yun, S.-G. Nam, M. Son, D. S. Lee, D. C. Kim, S. Seo, H. C. Choi, H.-J. Lee, S. W. Lee, and J. S. Kim, Breakdown of the interlayer coherence in twisted bilayer graphene, *Phys. Rev. Lett.* **110**, 096602 (2013).
- [20] V. Perebeinos, J. Tersoff, and P. Avouris, Phonon-mediated interlayer conductance in twisted graphene bilayers, *Phys. Rev. Lett.* **109**, 236604 (2012).
- [21] A. Rozhkov, A. Sboychakov, A. Rakhmanov, and F. Nori, Electronic properties of graphene-based bilayer systems, *Phys. Rep.* **648**, 1 (2016).
- [22] P. Moon and M. Koshino, Optical absorption in twisted bilayer graphene, *Phys. Rev. B* **87**, 205404 (2013).
- [23] E. J. Mele, Commensuration and interlayer coherence in twisted bilayer graphene, *Phys. Rev. B* **81**, 161405 (2010).
- [24] E. J. Mele, Interlayer coupling in rotationally faulted multilayer graphenes, *J. Phys. D: Appl. Phys.* **45**, 154004 (2012).
- [25] K. J. U. Vidarte, F. P. Rizzo, E. S. Morell, and C. Lewenkopf, Stoner ferromagnetism in low-angle twisted bilayer graphene at three-quarters filling, *Phys. Rev. B* **111**, 045164 (2025).
- [26] S. Plimpton, Fast parallel algorithms for short-range molecular dynamics, *J. Comput. Phys.* **117**, 1 (1995).
- [27] I. Leven, I. Azuri, L. Kronik, and O. Hod, Inter-layer potential for hexagonal boron nitride, *J. Chem. Phys.* **140**, 104106 (2014).
- [28] I. Leven, T. Maaravi, I. Azuri, L. Kronik, and O. Hod, Interlayer potential for graphene/h-bn heterostructures, *J. Chem. Theory Comput.* **12**, 2896 (2016).
- [29] T. Maaravi, I. Leven, I. Azuri, L. Kronik, and O. Hod, Interlayer potential for homogeneous graphene and hexagonal boron nitride systems: Reparametrization for many-body dispersion effects, *J. Phys. Chem. C* **121**, 22826 (2017).
- [30] W. Ouyang, D. Mandelli, M. Urbakh, and O. Hod, Nanoserpents: Graphene nanoribbon motion on two-dimensional hexagonal materials, *Nano Lett.* **18**, 6009 (2018).
- [31] J. Tersoff, New empirical approach for the structure and energy of covalent systems, *Phys. Rev. B* **37**, 6991 (1988).
- [32] A. Kinacı, J. B. Haskins, C. Sevik, and T. Çağın, Thermal conductivity of BN-C nanostructures, *Phys. Rev. B* **86**, 115410 (2012).
- [33] X. Liang, Z. A. H. Goodwin, V. Vitale, F. Corsetti, A. A. Mostofi, and J. Lischner, Effect of bilayer stacking on the atomic and electronic structure of twisted double bilayer graphene, *Phys. Rev. B* **102**, 155146 (2020).
- [34] N. N. T. Nam and M. Koshino, Lattice relaxation and energy band modulation in twisted bilayer graphene, *Phys. Rev. B* **96**, 075311 (2017).
- [35] K. J. U. Vidarte and C. Lewenkopf, High-energy Landau levels in graphene beyond nearest-neighbor hopping processes: Corrections to the effective Dirac Hamiltonian, *Phys. Rev. B* **106**, 155414 (2022).
- [36] K. J. U. Vidarte and C. Lewenkopf, Quasicrystalline 30° twisted bilayer graphene: fractal patterns and electronic localization properties, *Front. Carbon* **3**, 1496179 (2024).
- [37] J. Bardeen, Tunnelling from a many-particle point of view, *Phys. Rev. Lett.* **6**, 57 (1961).
- [38] A. D. Gottlieb and L. Wesoloski, Bardeen's tunnelling theory as applied to scanning tunnelling microscopy: a technical guide to the traditional interpretation, *Nan-*

- otechnology **17**, R57 (2006).
- [39] E. Y. Andrei, G. Li, and X. Du, Electronic properties of graphene: a perspective from scanning tunneling microscopy and magnetotransport, *Rep. Prog. Phys.* **75**, 056501 (2012).
- [40] J. Tersoff and D. R. Hamann, Theory and application for the scanning tunneling microscope, *Phys. Rev. Lett.* **50**, 1998 (1983).
- [41] J. Tersoff and D. R. Hamann, Theory of the scanning tunneling microscope, *Phys. Rev. B* **31**, 805 (1985).
- [42] O. Fischer, M. Kugler, I. Maggio-Aprile, C. Berthod, and C. Renner, Scanning tunneling spectroscopy of high-temperature superconductors, *Rev. Mod. Phys.* **79**, 353 (2007).
- [43] S. Hembacher, F. J. Giessibl, J. Mannhart, and C. F. Quate, Revealing the hidden atom in graphite by low-temperature atomic force microscopy, *Proc. Natl. Acad. Sci. U.S.A.* **100**, 12539 (2003).